2024 International Conference on Manipulation, Automation and Robotics at Small Scales (MARSS) | 979-8-3503-7680-7/24/$31.00 ©2024 IEEE | DOI: 10.1109/MARSS61851.2024.10612739

# Fin-Wave-Inspired Wireless Small-Scale Soft Robot for Adaptive Amphibious Locomotion under Single-Mode Magnetic Field

Chen Wang, Sarthak Misra, and Venkatasubramanian Kalpathy Venkiteswaran

***Abstract*— Magnetic soft robots are capable of generating programmable deformation based on variable magnetization profiles, with the added potential advantages of easy fabrication and miniaturization. However, achieving efficient locomotion and maneuverability in complex and variable environments often requires intricate modulation of external magnetic field which limits their applications. Inspired by the undulating fin-wave often seen in aquatic organisms, this paper demonstrates a small-scale soft robot capable of adaptive amphibious locomotion under a rotating magnetic field, allowing the robot to efficiently move on the solid surface (dry) and in liquids (wet). The robot comprises of a combination of multiple soft rod-shaped legs (6×1×1 mm) with different magnetization directions capable of generating undulating waves. Simulation of the undulating wave is conducted based on Cosserat rod theory to aid in the design and arrangement of the legs. The maneuverability and capability of steering and transitioning from dry to wet surfaces as well as sinking and floating in hybrid environments are demonstrated. The robot's ability to move with and against the flow of liquid in pipes of variable diameter is studied and characterized. The results demonstrate the potential to use as a small-sized wireless robot in applications, such as navigating within human blood vessels for clinical interventions.**

## I. Introduction

Magnetically-actuated soft robots are foreseen to have a profound impact on medical applications, especially in minimally invasive surgery (MIS) [1]–[3]. As medical robots, their soft, untethered, miniaturized bodies offer greater capability for reaching confined and enclosed spaces within the human body in comparison to their tethered and rigid counterparts [4]–[9]. However, unstructured environments and a combination of liquid and solid interfaces are common in the areas of interest where robots need to operate, such as within the human body. Existing magnetic soft robots typically perform a single mode of locomotion either in liquid or on solid substrates under a simple external magnetic field [10]–[13]. Despite numerous studies highlighting the multi-modal locomotion capabilities of their robots, controlling and switching motion modes still necessitates complex external magnetic fields [14, 15]. The potential applications could greatly benefit from simplified actuation magnetic field requirements while maintaining motion efficiency.

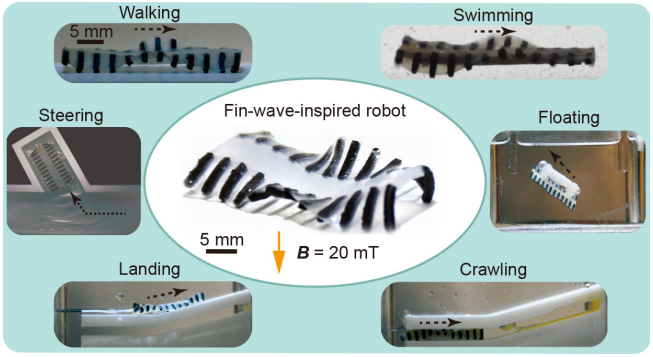


**Fig. 1:** The fin-wave-inspired soft robot and examples of the robot's amphibious locomotion abilities in different media (e.g. water, oil, dry PLA surfaces) and environments (e.g. on dry and wet surfaces, underwater, narrow channel) under the actuation of rotating magnetic field (***B***). The dashed arrows indicate the directions of the robot motion.

Unlike terrestrial robots (e.g. quadruped [12, 16, 17], millipede [18]–[21]) and swimming robots (e.g. sperm bots [22, 23], the helical swimmers [8, 24]) that primarily specialize in either ground or water-based locomotion, robots with amphibious locomotion capabilities excel in both aquatic and terrestrial environments. This versatility grants them access to a wider range of settings, enhancing their overall adaptability [25]. Generally, amphibious robot designs can be classified into three categories based on their propulsion mechanisms and structural features: wheeled, legged, and undulating [26, 27]. Notably, legged robots lacking palmate feet usually struggle to swim [28, 29], while those with palmate feet can swim but face challenges related to complex controller design and limited efficiency in terrestrial movement [30]. Prior research on sheet-shaped magnetic robots has showcased their ability to perform diverse forms of locomotion, including swimming in liquids, rolling, walking, and crawling on solid surfaces in response to changes in the direction of a rotating magnetic field [6, 31]. An origami-inspired robot has also demonstrated the ability to roll and flip on the ground and swim in water [14]. However, they do rely on a high degree of control over the applied magnetic field to adjust the locomotion mode based on the environment. This places significant constraints on the actuation system and causes difficulties when scaling to application requirements.

The undulating wave propulsion mechanism has undergone extensive research and finds widespread application in the design of macro-sized amphibious robots [32]–[35]. Inspired

This work is supported by the European Research Council (ERC) under the European Union's Horizon 2020 Research and Innovation programme under Grant 866494 project – MAESTRO, and financial support from the China Scholarship Council (CSC).

Chen Wang and Sarthak Misra are with Surgical Robotics Laboratory, Department of Biomaterials and Biomedical Technology, University of Groningen and University Medical Centre Groningen, 9713 GZ Groningen, The Netherlands.

Sarthak Misra and Venkatasubramanian Kalpathy Venkiteswaran are with Surgical Robotics Laboratory, Department of Biomechanical Engineering, University of Twente, 7500 AE Enschede, The Netherlands.

Contact: c.wang@umcg.nl

by stingrays and squids, Festo introduced the 'BionicFinWave' in 2018, an amphibious robot with the capability to swim and land [36]. Liu *et al.* conducted experiments to investigate swimming performance, focusing on factors such as undulating frequency and fin wavelength [37]. In the meanwhile, Zhang *et al.* calculated optimal thrust and efficiency for undulating fin waves with varying geometrical parameters, utilizing computational fluid dynamics [38]. Building on these studies, the use of magnetic actuation to produce fin-wave propulsion will allow translating these concepts to small-scale wirelessly-driven amphibious soft robots.

This paper introduces a fin-wave-inspired small-scale magnetic soft robot capable of locomotion in liquids and on solid surfaces. The key feature of this robot is its adaptive amphibious locomotion under a single mode of actuation magnetic field, facilitating ease of actuation and control. This capability enables seamless transitions between aquatic and terrestrial environments. Additionally, the robot can achieve both sinking and floating on command with a phase-changing capsule embedded in its body. We employ Cosserat rod theory to analyze the motion of magnetic elements, aiding in the miniaturized robot design. Through experimental demonstrations, we showcase the robot motion capabilities and adaptability, highlighting its potential applications in clinical settings, such as within blood vessels. In comparison to existing magnetic soft robots, our presented robot offers several advantages, including amphibious locomotion ability, ease of control, high frequency actuation, maneuverability, and the potential to carry payloads.

## II. Materials and Methods

Inspired by swimming mechanisms in nature creatures like stingrays and squids, we use rhythmic magnetization changes to generate undulating waves. Two rows of magnetic rod-shaped legs are embedded along the sides of an unmagnetized soft body. These legs exhibit distinct deformations when exposed to a magnetic field, forming an undulating wave. On solid ground, the robot walks using these magnetic rod-shaped legs, while in aquatic environments, a thin soft film connecting the legs transforms them into a fin-wave, enabling swimming.

### A. Design

The design and dimensions of the fin-wave-inspired amphibious magnetic soft robot are depicted in the left image of Fig. 2(a). Symmetrically assembled on both sides of the robot body are two rows of legs shaped as rectangular rods, each measuring $6 \times 1 \times 1\text{mm}$. A thin 0.5 mm film connects these legs, facilitating swimming capabilities. The legs are labeled from $L1$ to $L12$ along the long x-axis under the coordinate system, as illustrated in Fig. 2(a). The magnetization directions undergo continuous 45° changes between adjacent/successive legs, as depicted on the right side of Fig 2(a). Notably, these alterations in the magnetic dipoles of the legs occur within the yz plane while the actuation magnetic field rotates within the xz plane about the y-axis.

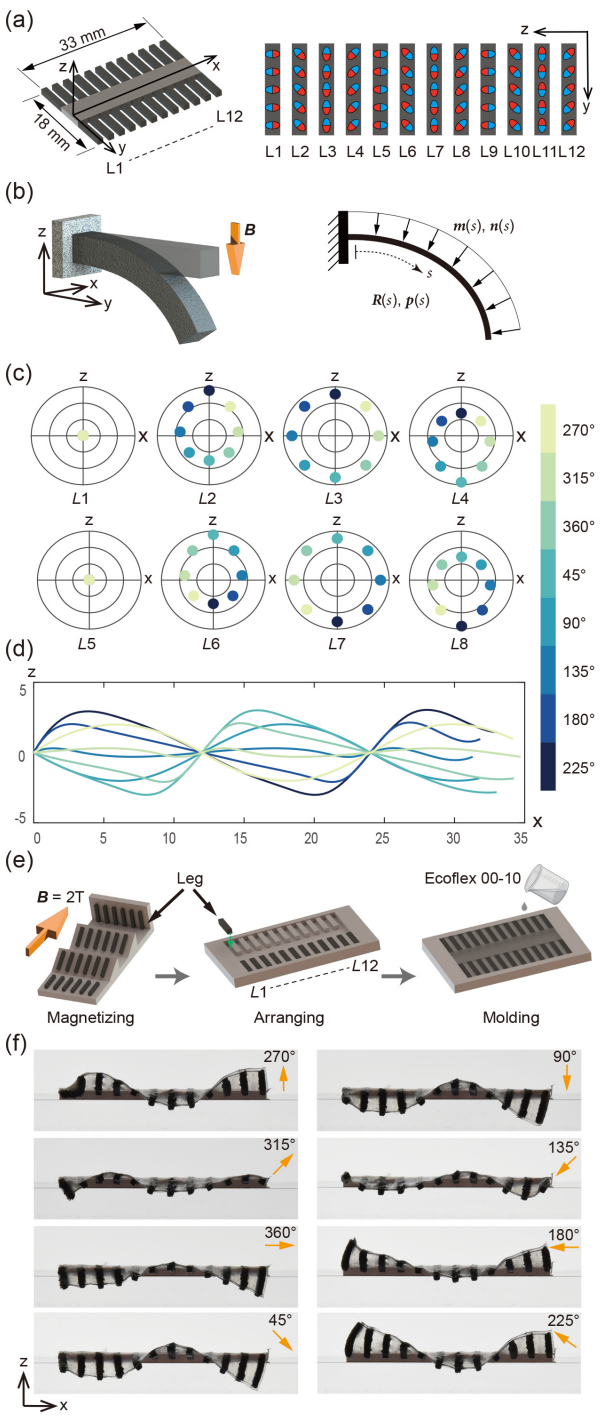


**Fig. 2:** Design, modeling and fabrication of the soft robot. (a) Design of the robot and the magnetization directions within the legs (labeled ($L1$-$L12$)). (b) Each individual leg is conceptualized as an elongated rod, anchored at one end to the robot body, and its actuation response modeled using Cosserat rod theory. $\boldsymbol{R}(s)$, $\boldsymbol{p}(s)$, $\boldsymbol{n}(s)$ and $\boldsymbol{m}(s)$ are material states vectors at the position $s \in [0, l]$ along the rod. (c) The positions of the distal tips of legs 1-8 (labeled as ($L1$-$L8$)), with a color bar indicating orientation of magnetic field to the x-axis. (d) Fin waves obtained by connecting the tips of all 12 legs under varying magnetic field directions. (e) The fabrication procedure goes from magnetization of individual legs to arrangement in a mold for the forming of robot body and fin. (f) Experimental results at 30 mT showing the fin wave on one side of the robot. The yellow arrows indicate the directions of the magnetic field.

### B. Materials

The robot's legs are constructed from a magnetic polymer composite (MPC) that responds to external magnetic fields, whereas the body and fin film are composed of silicone rubber without magnetic particles. The MPC comprises a silicone rubber matrix (Ecoflex-0010, Smooth-On Inc., USA) and a ferromagnetic powder of praseodymium-iron-boron (PrFeB) with a mean particle size of 5$\mu$m (MQFP-16-7-11277, Magnequench GmbH, Germany). In this study, a 1:1 mass ratio of magnetic microparticles to silicone rubber is employed. The MPC exhibits a relatively low elastic modulus of 2 MPa and 300% elongation at break, conferring a soft and flexible internal structure to the robot.

### C. Modeling

To elucidate the arrangement of the robot legs and delve into the dynamics of its waveform, we employ a model grounded in Cosserat-rod theory. In this model, an individual leg of the robot is conceptualized as a flexible rod, firmly attached at its proximal end to a rigid base and free to move at its distal tip. Fig. 2(b) provides a schematic illustration of how the leg bends under the influence of the magnetic field. This Cosserat-rod model is coupled with magnetization profiles and magnetic fields, enabling us to simulate the deformation of the legs. Here, each rod is characterized by its centerline curve in three-dimensional space, denoted by $s \in [0, l]$, where $l \in \mathbb{R}^3$ represents the length of the leg. The discretized cross-section along $s$ can be succinctly expressed by a material state vector:

$$\boldsymbol{y}(s) = [\boldsymbol{R}(s)\ \boldsymbol{p}(s)\ \boldsymbol{n}(s)\ \boldsymbol{m}(s)], \tag{1}$$

where $\boldsymbol{R}$ is rotation matrix of material orientation, $\boldsymbol{p}$ represents global position in Cartesian coordinates, $\boldsymbol{n}$ is internal force in the global frame, $\boldsymbol{m}$ represents internal moment in the global frame.

The actuation magnetic field is generated using 3D electromagnetic coils designed to produce a uniform magnetic field within the workspace, and therefore the contribution of the magnetic field gradient is assumed to be negligible [39]. Consequently, the applied force distribution per unit of s is denoted as $\boldsymbol{f}(\mathrm{s}) = 0$. Additionally, for the purposes of this study, gravity is disregarded. Therefore, the applied torque distribution per unit length of $s$ can be represented as ($\boldsymbol{q} \in \mathbb{R}^3$), and is given by

$$\boldsymbol{q}(s) = \mu \times \boldsymbol{B}\ , \tag{2}$$

where $\mu \in \mathbb{R}^3$ is the magnetic dipole moment per unit, $\boldsymbol{B} \in \mathbb{R}^3$ is the magnetic field. Thus the equilibrium differential equations are expressed as:

$$\dot{\boldsymbol{n}}(s) + \boldsymbol{f}(s) = 0\ , \tag{3}$$

$$\dot{\boldsymbol{m}}(s) + \dot{\boldsymbol{p}}(s) \times \boldsymbol{n}(s) + \boldsymbol{q}(s) = 0\ , \tag{4}$$

where the dot denotes a derivative with respect to $s$.

The boundary value problem of Cosserat rod is solved using the fourth-order Runge-Kutta method, implemented using Matlab (2021a, Mathworks, USA). The detailed modeling and solution approach closely adhere to the methodologies outlined in [40, 41], and implementation details can be found in our previous work [42].

To set the robot in motion, a magnetic field is provided in the xz plane, rotating about y-axis. In the model, eight different orientation of the magnetic field are considered within one actuation cycle (0°-360°) with a spacing of 45°. Due to variations in magnetization, each leg undergoes distinct deformations. The 12 legs on one side of the robot are defined as $L1$-$L12$. The positions of the distal tips of $L1$ to $L8$ on the xz plane under different magnetic field directions are presented in Fig. 2(c). Notably, $L2$-$L4$ and $L6$-$L8$ move in circular patterns, with varying amplitudes and phase shifts. By contrast, $L1$ and $L5$ predominantly experience twisting, resulting in fixed tip positions on the xz plane. By connecting the tips of $L1$ to $L12$, an fin-like dynamic waveform emerges, as depicted in Fig. 2(d). The simulation results showing undulating fin-like waves with magnitude changing and phase shift that theoretically can generate thrust in liquid environment as verified in [37, 38]. Also, the circular motion path of $L2$-$L4$ and $L6$-$L8$ have potential to generate movement on solid ground as demonstrated in [12]. Experimental results showcasing the generation of this fin-wave under a rotating magnetic field at 30 mT are featured in Fig. 2(f). It is worth noting that variations in the movement of individual legs in the experiment compared to simulation results may arise from factors such as the influence of gravity on the legs themselves and the presence of the thin film connecting the legs.

### D. Fabrication

The fabrication procedure is detailed in Fig. 2(e). Initially, 3D printed PLA molds are employed to shape the robot's legs. Subsequently, the magnetic polymer composite (MPC) undergoes a degassing process and is allowed to cure naturally at room temperature (24°C) for four hours. Once cured, the MPC legs are arranged within a specialized fixture and exposed to a 2 T magnetic field, achieved using an impulse magnetizer (ASC Model IM-10-30, ASC Scientific, USA), to obtain the desired magnetization profile. These magnetized legs are then transferred to another mold, where they are systematically repositioned according to the order derived from simulation results. Finally, silicone rubber is cast into these molds, resulting in the formation of the robot body and the interconnecting fin.

## III. Experiments and Results

To demonstrate the capability and maneuverability of robot locomotion, experiments are carried out in different environments shown in the following sections.

### A. Amphibious Locomotion

The robot's amphibious locomotion capabilities are demonstrated across various media: on solid ground (3D printed PLA surface), on the surface of water, underwater, and at the oil-water interface (as shown in Fig. 3 (a)-(d), **please refer to supplementary video**). Fig. 3 (I) displays the robot

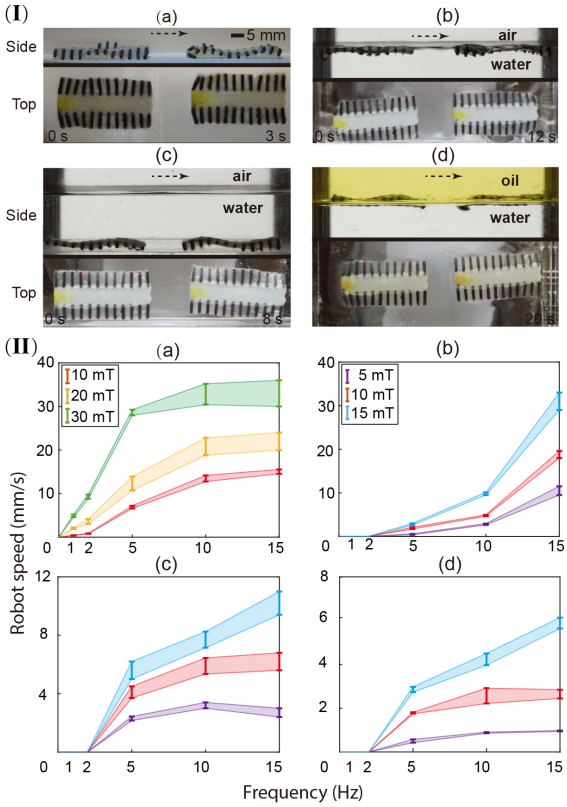


**Fig. 3:** Demonstration and characterization of the locomotion and speed in different media: (I): Demonstration of basic locomotion abilities of the robot. (a) Walking on solid surface (PLA). (b) Swimming on the surface of water. (c) Motion on underwater ground. (d) Swimming between the interface of water and oil. A magnetic field of 10mT rotating at 15 Hz is used in the demonstrations. The dashed arrows indicate the directions of the robot motion. (II): Characterization of robot locomotion speed in the abovementioned four media under different magnitude and frequency of rotating magnetic field. (**please refer to supplementary video**)

postures from both top and side views at different time points in these environments.Accordingly, the motion velocities in these four media were measured under varying magnitudes and frequencies of the rotating magnetic field as shown in Fig. 3 (II). Each experiment was repeated three times to obtain average data and assess errors. It can be observed that the velocity in all media increases with the increases of magnetic frequency and/or magnetic field strength. When comparing the red lines (magnetic field at 10 mT and 10 Hz) in Fig. 3 (II), walking demonstrates higher efficiency than swimming. Swimming is most efficient on the water surface, while it is slower at the oil and water interface. Walking on solid ground requires magnetic fields between 10 mT and 30 mT, while swimming demands lower field strengths (5 mT) but no higher than 15 mT for stable movement. Lower magnetic frequencies (1 mT and 2 mT) support walking on solid ground but not swimming. Higher magnetic frequencies enhance swimming more than walking, whereas greater field magnitudes improve walking more than swimming. These trends serve as guidelines for subsequent experiments involving special maneuvers.

### *B. Maneuverability and capability*

In addition to its fundamental amphibious locomotion, the robot possesses the capability to execute specialized maneuvers, enabling it to navigate complex environments. Steering is achieved by adjusting the tilt angle between the plane of the rotating magnetic field and the xz plane (as defined in Fig. 2(a)). Altering this tilt angle induces a phase difference between the fins on either side of the body, prompting the robot to align with the plane of rotation of the magnetic field, resulting in turning [18]. The direction of turning, whether left or right, can be changed by reversing the tilt angle. Experiments to demonstrate the robot maneuverability on both solid ground and water surfaces are conducted and depicted in Fig. 4 (a) and (b), respectively (**please refer to supplementary video**).

In Fig. 4(c), the robot's navigational prowess within a tube with a two-way fork is highlighted. Initially, it travels straight from the right end to the left end and returns. Then, it turns at a $60^\circ$ angle, entering the side channel. Fig. 4(d) shows the robot's successful traversal of an extremely narrow 2 mm-high channel under a rotating magnetic field at 10 mT and 10 Hz. Capabilities of transition from swimming in deep water to landing on a dry slope are demonstrated in Fig. 4(e) and Fig. 4(f), both in open space and within a 5 mm-high narrow channel. Importantly, these transitions between water and solid ground are reversible (**please refer to supplementary video**).

Additionally, we also show that the robot can be altered to control its ballast for sinking or floating in liquid environments. A 2 mL acetone capsule is embedded onto the top surface of the robot body. This capsule is constructed from a rigid PE (Polyethylene) hollow pipe, with acetone injected into it using a syringe and sealed with thin silicone rubber films at both ends. Acetone has a low boiling point of $56^\circ$, and undergoes a phase change from liquid to gas when the temperature surpasses this critical value. Consequently, the capsule inflates upon heating, increasing the robot's volume and altering its buoyancy. The robot can float when the environmental temperature exceeds 56°C and sink when the temperature drops below this critical temperature. Fig. 5 demonstrates the robot moving underwater with the embedded capsule (also acting as payload), followed by floating and motion on water surface, and subsequently sinking again (**please refer to supplementary video**). A pump is used to control the water temperature, facilitating heating and cooling, thus enabling repeated rounds of sinking and floating experiments to illustrate the repeatability of the acetone capsule (**please refer to supplementary video**).

### *C. Applications*

Based on the robot's capabilities, a possible area of application is inside the human body, where such robots can potentially be used for surgical interventions by navigating blood vessels or other body conduits. To explore such potential clinical applications, experiments were conducted within fluid-filled circular pipes that mimic conditions found in blood vessels. Two pipes, one with a 22 mm diameter

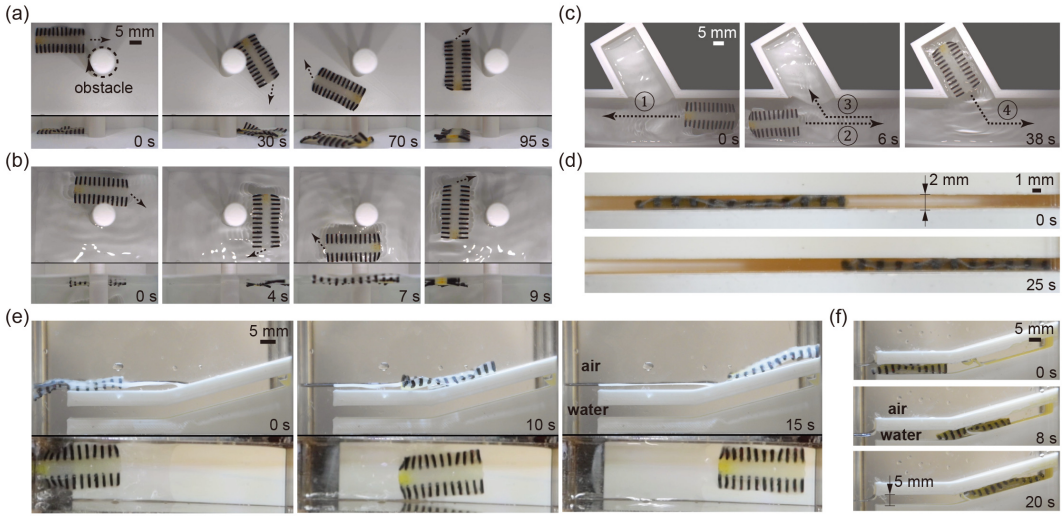


**Fig. 4:** Demonstrations of robot maneuverability and capability: (a) The robot is steered to walk around a pillar/obstacle (Magnetic field: ($|\boldsymbol{B}|$ = 10 mT), frequency: ($f$ = 1 Hz)). (b) The robot is steered to swim around a pillar on water surface ($|\boldsymbol{B}|$ = 10 mT, $f$ = 10 Hz). (c) The robot can be controlled to select the target path at a fork while swimming ($|\boldsymbol{B}|$ = 10 mT, $f$ = 10 Hz). (d) The robot is crawling in a 2 mm height narrow channel ($|\boldsymbol{B}|$ = 10 mT, $f$ = 10 Hz). (e) Demonstration of the robot transitioning from water to ground ($|\boldsymbol{B}|$ = 30 mT, $f$ = 5 Hz). (f) The robot switches between water and ground in a 5 mm height channel ($|\boldsymbol{B}|$ = 30 mT, $f$ = 5 Hz). The dashed arrows indicate the direction of the robot motion (**please refer to supplementary video**).

(Fig. 6(a)) and another with a 16 mm diameter (Fig. 6(b)), are used to assess the robot's adaptability (with the robot width measuring 18 mm). Motion within the pipe was observed using cameras (top and side views) and ultrasound (US) imaging with a transducer ((SonixTouch Q+, BK Medical, Quickborn, Germany, shown in Fig. 6 (c) and (d)). Pulsatile flow was generated using a pump (HV-77 910-55, Masterflex, Illinois, USA), and the flow rate was adjustable, with actual flow rates visualized and measured using Doppler data from the US device (Fig. 6(d)). Motion velocities of the robot, both with and against the flow, were measured in both the large and narrow pipes under different flow velocities, as depicted in Fig. 6 (e) and (f). Generally, the robot moves slower in the narrow pipe compared to the larger one. Additionally, it is observed that motion velocity along the flow direction increased with the flow velocity rise in the larger pipe, while motion against the flow direction decreased with increasing flow velocity. In the narrow pipe, the moving fluid assisted motion in the flow direction, but had minimal impact on motion speed when moving against the flow.

### *D. Discussion*

The experimental results support the predicted undulating wave from simulations. By manipulating the directions of the magnetic field, we observed corresponding changes in the motion of the legs, resulting in undulating fin-waves with variations in magnitude and phase shifts. While the simulation and experimental fin-waves appear similar, it is worth noting that no quantitative comparisons were conducted in this study. The primary purpose of the simulations in this paper was to provide information regarding the leg arrangement required to achieve the desired undulating wave for amphibious locomotion. The optimization of motion efficiency, including aspects like robot body shape and the number of legs, has been explored in other research studies [37, 38], and is not considered this study.

The characterization of amphibious locomotion across various terrains, including solid ground, water surface, underwater, and at the oil-water interface, has been conducted. The actuation threshold for walking on solid ground ranged from 10 mT to 30 mT, while swimming in water required a lower magnetic field strength, starting from 5 mT and going up to 15 mT. The higher threshold for walking is attributed to the robot body weight, necessitating greater actuation force compared to swimming, where buoyancy offsets gravity. The magnetic fields exceeding 30 mT during walking caused the robot to roll up, while fields higher than 15 mT during swimming on the water surface led to the robot flipping over. Additionally, it is important to note that the efficiency of forward and backward motion varies due to differences in the magnetization profiles of the robot legs, but this discrepancy does not impact the robot amphibious locomotion abilities. The motion velocities presented in Fig. 3 II are characterized in the same direction of motion for consistency and clarity.

The use of an acetone capsule for adjusting the buoyancy of the robot is a cost-effective approach for the current experiments. However, it is essential to explore biocompatible materials for potential medical applications in the future. One promising candidate is Novec 7000 Engineered Fluid (3M, USA), which has a boiling point at 34°C, enabling phase changes at lower temperatures. In medical scenarios, it is impractical to heat the material by pumping hot water, so alternative methods need to be considered. One possibility is incorporating a phase-changing material mixed with mineral powder, allowing the temperature of the material to be remotely raised via RF heating [43]. Additionally, integrating the buoyancy capsule with the robot body can be considered for miniaturization, enhancing its suitability for clinical applications.

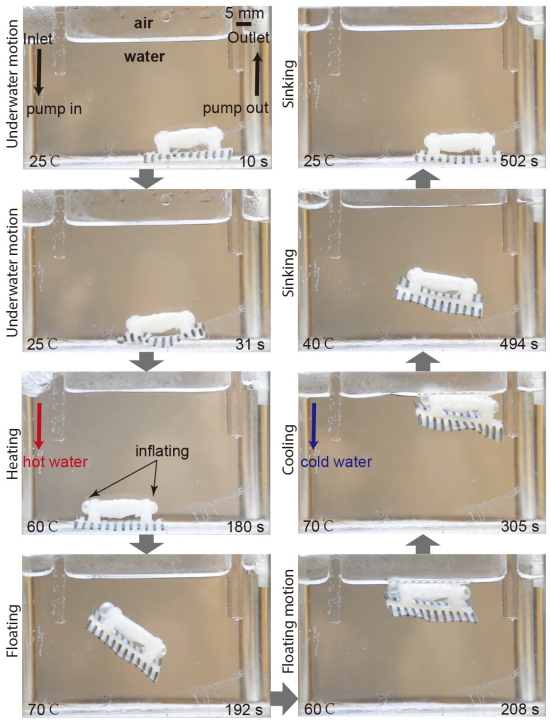


**Fig. 5:** Demonstration of the robot sinking and floating in water (side view). The robot embedded with a buoyancy capsule is controlled to move underwater, float up to water surface, swim on water surface and sink again to reach the starting point. A pump is connected to the inlet on the left corner and and outlet on right corner of the tank setup, allowing injection of hot and cold water for the heating and cooling of the environment. (**please refer to supplementary video**)

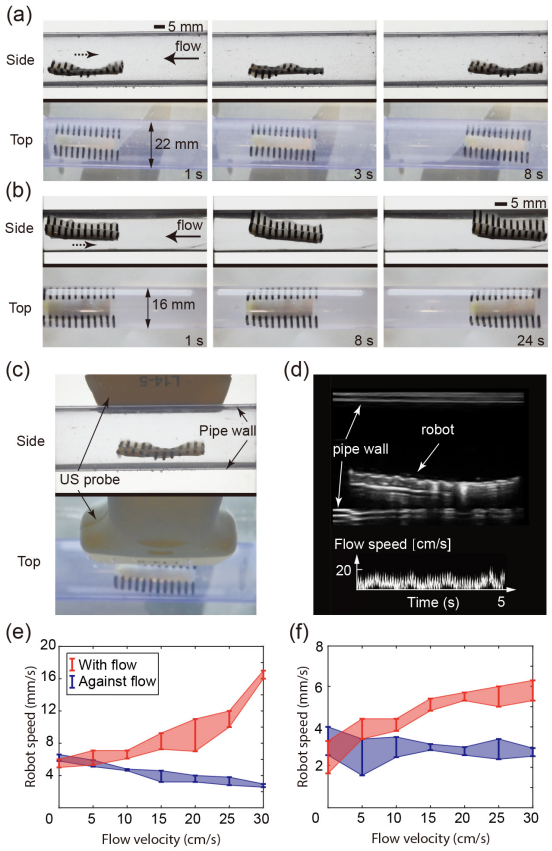


**Fig. 6:** Demonstration and characterization of robot motion in pipes with flowing water. (a) The robot moving in a 22 mm diameter pipe. (b) The robot moving in a 16 mm diameter pipe. (c) Robot motion is observed via both camera and ultrasound (US) probe. (d) US image when the robot is moving in the big pipe. The flow velocity is visualized and measured using Doppler mode. (e) Robot speed in the 22 mm pipe under different flow velocities. (f) Robot speed in the 16 mm pipe under different flow velocities. Magnetic field for all the above experiments are 20 mT at a frequency of 10 Hz. The dashed arrows indicate the directions of the robot motion (**please refer to supplementary video**).

The motion ability of propulsion within pipes with flowing water indicates that the robot has potential to be utilized in blood vessels for clinical applications. The robot developed in this study can perhaps navigate some of the larger blood vessels within the human body, but needs to be miniaturized for more general use. This may be possible by using lithography to make the molds at a smaller scale [44]. If miniaturized, the robot can execute clinical tasks such as drug delivery and biosensing [45, 46]. Further research into navigation in complex conduit networks or a blood vessel phantom is needed. Additionally, closed loop control with tracking of the robot's position and orientation is essential for practical applications.

## IV. Conclusions and Future Work

This study demonstrates the unique amphibious locomotion capabilities and potential applications of a multi-legged small-scale magnetic soft robot inspired by fin-wave movement—a novel feature not previously shown in magnetic soft robots. The robot exhibits fin-wave locomotion on solid ground, water surface, underwater, and even at oil-water interfaces, showcasing its adaptability across diverse media. The robot is capable of locomotion in different media under a single-mode magnetic actuation, simplifying the control of motion. The design of the robot and arrangement of the magnetic legs are informed by simulation results. Experimental results highlight its abilities, including sinking and floating, landing, maneuvering through narrow channels, and navigating in pipes with flowing liquid. Notably, each individual leg on the robot is a simple rectangular rod, facilitating facile fabrication and offering the possibility of scaling down the overall size of the robot for potential miniaturization in clinical applications.

To facilitate future clinical applications, additional research efforts are essential to enhance the functionality of the robot. Exploring actuation and motion control using a rotating permanent magnet is essential for extending the operational range of the robot and expanding its potential applications. Building upon the current design and our prior research [39], it is feasible to integrate a magnetically-actuated capsule onto the robot, enabling functionalities like drug delivery and biopsy. Furthermore, the robot can serve as a hemostatic bandage by applying a chitosan coating to its body, forming robust bonds with mucosal surfaces, particularly in the gastrointestinal tract. Further miniaturization can be accomplished through technologies such as lithography and 3D printing, enabling the development of small-scale robot designs tailored to specific clinical tasks and applications.

## REFERENCES


[1] C. Laschi *et al.*, "Soft robotics: Technologies and systems pushing the boundaries of robot abilities," *Science Robotics*, vol. 1, no. 1, p. eaah3690, 2016.

[2] M. Tonutti *et al.*, "The role of technology in minimally invasive surgery: state of the art, recent developments and future directions," *Postgraduate Medical Journal*, vol. 93, no. 1097, pp. 159–167, 2017.

[3] C. Wang *et al.*, "Microrobots for minimally invasive medicine," *Annual Review of Biomedical Engineering*, vol. 12, pp. 55–85, 2010.

[4] J. Burgner-Kahrs *et al.*, "Continuum robots for medical applications: A survey," *IEEE Transactions on Robotics*, vol. 31, no. 6, pp. 1261–1280, 2015.

[5] Z. Li and E. Diller, "Multi-material fabrication for magnetically driven miniature soft robots using stereolithography," *Proceedings of the IEEE International Conference on Manipulation, Automation and Robotics at Small Scales (MARSS)*, pp. 1–6, 2022.

[6] W. Hu *et al.*, "Small-scale soft-bodied robot with multimodal locomotion," *Nature*, vol. 554, no. 7690, pp. 81–85, 2018.

[7] Y. Kim *et al.*, "Ferromagnetic soft continuum robots," *Science Robotics*, vol. 4, no. 33, p. eaax7329, 2019.

[8] S. Tottori *et al.*, "Magnetic helical micromachines: fabrication, controlled swimming, and cargo transport," *Advanced materials*, vol. 24, no. 6, pp. 811–816, 2012.

[9] J. Tian *et al.*, "Designing ferromagnetic soft robots (ferrosoro) with level-set-based multiphysics topology optimization," *Proceedings of the IEEE International Conference on Robotics and Automation (ICRA)*, pp. 10 067–10 074, 2020.

[10] S. Tottori *et al.*, "Magnetic helical micromachines: fabrication, controlled swimming, and cargo transport," *Advanced materials*, vol. 24, no. 6, pp. 811–6, 2012.

[11] C. Wang *et al.*, "A snake-inspired multi-segmented magnetic soft robot towards medical applications," *IEEE Robotics and Automation Letters*, vol. 7, no. 2, pp. 5795–5802, 2023.

[12] V. K. Venkiteswaran *et al.*, "Bio-inspired terrestrial motion of magnetic soft millirobots," *IEEE Robotics and Automation Letters*, vol. 4, no. 2, pp. 1753–1759, 2019.

[13] A. Bhattacharjee *et al.*, "Untethered soft millirobot with magnetic actuation," *Proceedings of the IEEE International Conference on Robotics and Automation (ICRA)*, pp. 3792–3798, 2020.

[14] Q. Ze *et al.*, "Spinning-enabled wireless amphibious origami millirobot," *Nature Communications*, vol. 13, no. 1, p. 3118, 2022.

[15] Z. Ren *et al.*, "Soft-bodied adaptive multimodal locomotion strategies in fluid-filled confined spaces," *Advanced Science*, vol. 7, no. 27, p. eabh2022, 2021.

[16] D. Rus and M. Tolley, "Design, fabrication and control of soft robots," *Nature*, vol. 521, no. 7553, pp. 467–475, 2015.

[17] R. Shepherd *et al.*, "Multigait soft robot," *Proceedings of the National Academy of Sciences of the United States of America*, vol. 108, no. 51, pp. 20 400–20 403, 2011.

[18] V. K. Venkiteswaran *et al.*, "Tandem actuation of legged locomotion and grasping manipulation in soft robots using magnetic fields," *Extreme Mech. Lett.*, vol. 41, no. 2, pp. 11 010–1023, 2020.

[19] Z. Cui *et al.*, "Miniaturized metachronal magnetic artificial cilia," *Proceedings of the National Academy of Sciences of the United States of America*, vol. 120, no. 35, p. e2304519120, 2023.

[20] T. Islam *et al.*, "Highly motile nanoscale magnetic artificial cilia," *Proceedings of the National Academy of Sciences of the United States of America*, vol. 118, no. 35, p. e2104930118, 2021.

[21] H. Gu *et al.*, "Magnetic cilia carpets with programmable metachronal waves," *Nature Communications*, vol. 11, no. 1, p. 2637, 2020.

[22] Z. Wang *et al.*, "Soft bio-microrobots: Toward biomedical applications," *Advanced Intelligent Systems*, vol. 6, no. 2, p. 2300093, 2023.

[23] K. Zhang *et al.*, "Locomotion of bovine spermatozoa during the transition from individual cells to bundles," *Proceedings of the National Academy of Sciences of the United States of America*, vol. 120, no. 3, p. e2211911120, 2023.

[24] C. Li *et al.*, "Closed-loop control characterization of untethered small-scale helical device in physiological fluid with dynamic flow rates," *Advanced Intelligent Systems*, vol. 5, no. 5, p. 2200322, 2023.

[25] Z. Cheng *et al.*, "A highly robust amphibious soft robot with imperceptibility based on a water-stable and self-healing ionic conductor," *Advanced materials*, vol. 35, no. 28, p. 2301005, 2023.

[26] R. Baines *et al.*, *Amphibious robotic propulsive mechanisms: Current technologies and open challenges*. Bioinspired sensing, actuation, and control in underwater soft robotic systems, 2021.

[27] K. Ren and J. Yu, "Research status of bionic amphibious robots: A review," *Ocean Engineering*, vol. 227, p. 108862, 2021.

[28] S. Yoo *et al.*, "Design and analysis of carbon fiber reinforced plastic body frame for multi-legged subsea walking robot," *Ocean Engineering*, vol. 102, pp. 78–86, 2015.

[29] H. Lu *et al.*, "A bioinspired multilegged soft millirobot that functions in both dry and wet conditions," *Nature Communications*, vol. 9, no. 1, p. 3944, 2018.

[30] G. Wang *et al.*, "Subsea crab bounding gait of leg-paddle hybrid driven shoal crablike robot," *Mechatronics*, vol. 48, pp. 1–11, 2017.

[31] Z. Ren *et al.*, "Multi-functional soft-bodied jellyfish-like swimming," *Nature Communications*, vol. 10, no. 1, p. 2703, 2019.

[32] A. Ijspeert *et al.*, "From swimming to walking with a salamander robot driven by a spinal cord model," *Science*, vol. 315, no. 5817, pp. 1416–1420, 2007.

[33] K. Low, "Modelling and parametric study of modular undulating fin rays for fish robots," *Mechanism And Machine Theory*, vol. 44, no. 3, pp. 615–632, 2009.

[34] W. Chu *et al.*, "Review of biomimetic underwater robots using smart actuators," *International Journal of Precision Engineering*, vol. 12, pp. 1281–1292, 2012.

[35] A. McKee *et al.*, "Undulation frequency affects burial performance in living and model flatfishes," *Zoology*, vol. 119, no. 2, pp. 75–80, 2016.

[36] Festo. Bionicfinwave: Underwater robot with unique fin drive concept. [Online]. Available: https://www.festo.com/PDF_Flip/corp/Festo_BionicFinWave/en/index.html

[37] H. Liu and O. Curet, "Swimming performance of a bio-inspired robotic vessel with undulating fin propulsion," *Bioinspiration Biomimetics*, vol. 13, no. 5, p. 056006, 2018.

[38] Z. Yong-hua *et al.*, "Morphologic optimal design of bionic undulating fin based on computational fluid dynamics," *Proceedings of the IEEE International Conference on Robotics and Automation (ICRA)*, pp. 491–496, 2007.

[39] C. Wang *et al.*, "Biocompatible film-coating of magnetic soft robots for mucoadhesive locomotion," *Advanced Materials Technologies*, vol. 8, no. 12, p. 2201813, 2023.

[40] J. Till *et al.*, "Real-time dynamics of soft and continuum robots based on cosserat rod models," *International Journal Of Robotics Research*, vol. 38, no. 6, pp. 723–746, 2019.

[41] D. Rucker and R. Webster III, "Statics and dynamics of continuum robots with general tendon routing and external loading," *IEEE Transactions on Robotics*, vol. 27, no. 6, pp. 1033–1044, 2011.

[42] M. Richter *et al.*, "Multi-point orientation control of discretely-magnetized continuum manipulators," *IEEE Robotics and Automation Letters*, vol. 6, no. 2, pp. 3607–3614, 2021.

[43] Y. Tang *et al.*, "Wireless miniature magnetic phase-change soft actuators," *Advanced materials*, vol. 34, no. 40, p. 2204185, 2022.

[44] Z. Cui *et al.*, "Miniaturized metachronal magnetic artificial cilia," *Proceedings of the National Academy of Sciences of the United States of America*, vol. 120, no. 35, p. e2304519120, 2023.

[45] S. Wu and X. Zhao, "Tissue adhesive semiconductors," *Science*, vol. 381, no. 6658, pp. 608–609, 2023.

[46] C. Wang *et al.*, "In situ sensing physiological properties of biological tissues using wireless miniature soft robots," *Science Advances*, vol. 9, no. 23, p. eadg3988, 2023.